Circulation of hydraulically ponded turbidity currents in three-dimensional minibasins with implications for turbidite shape

J. Kevin Reece[1], Robert M. Dorrell[2], & Kyle M. Straub[1]

[1]Department of Earth and Environmental Sciences, Tulane University, New Orleans, LA 70118, U.S.A.

[2]Energy and Environment Institute, University of Hull, Hull, HU6 7RX, United Kingdom

Correspondence to: J. Kevin Reece (jreece@tulane.edu)

Abstract

Minibasins on continental margins trap turbidity currents transporting material downslope, but little is known about the inherently three-dimensional (3-D) mechanics of these confined flows. Utilizing new methodology, experimental results quantify flow dynamics in minibasins for the first time. It is shown that dynamics are dominated by 3-D circulation cell structures, across the fill-to-strip-to-spill transition that are controlled by flow discharge. Measurements of velocity throughout circulation cells indicate vorticity dominates strain rate with fluid rotating into the center of cells where it upwells: this influences minibasin sediment trapping potential and deposit heterogeneity. Flow properties link to depositional patterns on minibasin slopes. Specifically, higher input discharges are correlated with higher fluxes into the center of minibasins and reduced deposit tapering on minibasin slopes. This geometry is linked to the amount of sediment rich flow runup on the distal minibasin wall, where flow and sediment is delivered to circulation cells.

Introduction

Turbidity currents, a class of gravity flows that gain excess density by suspension of sediment, are the primary particulate transport process on the slope of continental margins [*Talling et al., 2015*]. These flows represent geohazards to submarine infrastructure, while also transporting particulate organic carbon and microplastics to deep marine reservoirs *[Carter et al., 2014; Hage et al., 2020; Pohl et al., 2020b; Sparkes et al., 2015*]. On many margins, turbidity currents encounter topographic obstacles including local depressions, seamounts, and shale ridges [*Nasr-Azadani & Meiburg, 2014; Straub & Mohrig, 2009; Völker et al., 2008*]. Depressions large enough to impact deposition from turbidity currents are often termed minibasins [*Mitchum Jr et al., 1977*]. Their ability to slow the progression of turbidity currents and sometimes hydraulically pond flows makes them hotspots for clastic sediment, particulate organic carbon, and microplastic accumulation [*Dorrell et al., 2018; Lamb et al., 2004; Pirmez et al., 2012; Prather et al., 2012*].

There is a lack of direct observations of field scale turbidity currents interacting with minibasins, primarily due to their: 1) relatively inaccessible locations, 2) unpredictable flow occurrences, and 3) high flow shear stresses that can destroy equipment [*Azpiroz-Zabala et al., 2017; Khripounoff et al., 2003*]. Development of theory has thus leveraged numerical and physical experiments [*Bastianon et al., 2021; Brunt et al., 2004; Toniolo et al., 2006b; Traer et al., 2018; Violet et al., 2005; Wang et al., 2017*]. However, due to computational demands, many numerical models utilize depth average flow parameters, limiting their applicability in settings where vertical flow properties vary strongly in space and time, such as in minibasins [*Meiburg et al., 2015; Yang et al., 2019*]. In addition, while a few physical experiments document flow interactions with topography in three-dimensions, 3-D, *[Maharaj, 2012; Soutter et al., 2021; Violet et al., 2005*], most physical experiments on turbidity current – minibasin interactions have been conducted in 2-D [*Lamb et al.*, 2004; *Patacci et al.*, 2015; *Pohl et al.*, 2020a; *Spinewine et al.*, 2009; *Toniolo et al.*, 2006b]. Ponding occurs due to a topographic obstacle, which triggers a rapid spatial flow deceleration to extremely low densimetric Froude conditions and the formation of a placid flow transition with the overlying ambient fluid, decreasing the entrainment of ambient fluid into the current [*Lamb et*

al., 2004; van Andel and Komar, 1969]. In 2-D (Fig. 1A), ponding produces concentration profiles with little vertical structure, as sediment lost to deposition is replaced from above with more sediment laden flow. This produces tabular deposits that do not rapidly thin against confining topography *[Lamb et al., 2004; Toniolo et al., 2006b*]. Flow circulation within 2-D minibasins was documented along a vertical plane, with a return flow positioned above down-basin directed flow [*Patacci et al., 2015*]. It is unclear if this style of circulation develops in 3-D minibasins.

We explore the influence of flow discharge into minibasins on the 3-D velocity field, structure of sediment concentration profiles, and turbidite shape. Flow discharge is adjusted by changing flow width, keeping all other input conditions constant. The setup is designed to capture endmembers across a minibasin fill-to-strip-to-spill transition [*Badalini et al., 2000; Beaubouef and Abreu, 2006; Beaubouef and Friedmann, 2000; Satterfield and Behrens, 1990; Winker, 1996*]. The campaign quantifies lateral circulation cells, which we link to upwelling flow that could impact sedimentation processes by countering the still fluid settling velocity of particles.

Experimental Design

Experiments were performed in a 6 x 4 x 2.2 m basin with an inner floor~~,~~ surrounded by moats. Circular minibasins were carved into 300 µm sand with a diameter of 3 m, 10% sidewall slopes, and a 0.12 m depth. Dimensionless ratios characterizing minibasin topography, including side wall slopes, fall within distributions generated from 2,324 depressions extracted from the Bureau of Ocean and Energy Management's bathymetric dataset of the northern Gulf of Mexico [*BOEM, 2017*]. Minibasins were submerged in fresh water with 0.69 m of water above the minibasin rim. Sustained turbidity currents were delivered to the rim of minibasins for 30 minutes. Input flows had densimetric Froude numbers of 1.1, were 48 mm thick, and had an excess density of 2.9%.

Our experiments utilized a novel aluminum oxide sediment (particle density of 3950 kg/m^3) of low cohesivity due to a deflocculant mixture containing calcium carbonate and sodium hexametaphosphate (SHMP) that was used to inhibit particle amalgamation. Volumetric sediment

concentration was 1% with D_5, D_{25}, D_{50}, D_{75}, D_{95} of 6, 11, 14, 17, and 24 μm, respectively. The high-density aluminum oxide sediment produces significant excess density from low volumetric sediment concentrations, generating swifter, more turbulent flows [*Fukuda et al., 2023*]. This allows transport of particles to greater distances prior to deposition, relative to experimental flows comprised of quartz sediment.

Three experiments were performed, each composed of two flow events, and are referred to as the low-flux (24 l/min & 65 mm entrance width), mid-flux (47.7 l/min & 130 mm width), and high-flux (96.9 l/min & 260 mm width) experiments. During the first event a 30 min long 3-component velocity profile timeseries was collected at minibasin center using a Pulse Coherent Acoustic Doppler Profiler (PCADP), in addition to equilibrium sediment concentration profiles collected 26 – 27.5 min into the flows. During the second event, velocity profiles were collected after equilibrium conditions were reached at a set of positions covering the river-left side of the minibasins. Topography was mapped with a displacement laser before and after each experiment.

Results

Minibasin center conditions

Equilibrium velocity conditions at minibasin center are estimated by averaging profiles collected from the first flow of each experiment over the duration that concentration profiles were collected. Here, *u, v,* and *w* refer to the velocity components in the down-basin, cross-basin, and vertical directions, respectively. For comparison, *u* velocity profiles at minibasin center are normalized by the maximum velocity of a profile, u_{max} (Fig. 2A). The low-flux condition has the most complicated velocity structure, with low velocities in the lower third of the flow, peak velocities in the middle third and a rapid velocity reduction in the upper third of the flow. The mid and high-flux conditions are less stratified and have peak velocities just below the minibasin rim elevation.

Sediment concentration profiles are compared following normalization by near bed conditions, C_{nb} (Fig. 2B). The low-flux experiment, which was the most contained within the minibasin, is the most stratified. The mid and high-flux conditions are well mixed in the lower two-thirds of the elevations contained within the minibasin. Sediment concentrations then rapidly decrease to near zero values approaching the rim elevation.

Evolution of down minibasin velocity

Experiments had differences in discharge, controlled by initial flow width, that generated different minibasin floor velocity due to varying lateral flow expansion (Fig. 2C) between experiments. All experiments show a rapid spatial deceleration in u_{max} with distance into the minibasin, as flow ponding triggered a rapid increase in flow height and decrease in densimetric Froude number. Minibasin floor velocities are used to estimate flow runup onto the distal minibasin wall. The magnitude of runup is estimated by:

$$\Delta z = \frac{\rho_c u_{max}^2}{(\rho_c - \rho_a) 2g} \qquad \textit{[EQ. 1]}$$

where ρ_c and ρ_a are current and ambient fluid densities and g is gravitational acceleration [*Dorrell et al., 2018; Straub et al., 2008*]. Here, ρ_c is estimated from measurements of sediment concentration. Use of Eq. 1 results in estimates of 3.9, 9.5, and 27.8 mm of runup for the low, mid, and high flux experiments, respectively. Finally, we note that measurements of u_{max} above the downstream minibasin rim indicate that the experiments captured the fill-to-strip-to-spill transition. The low-flux experiment (characterizing the "fill" endmember) has near zero u_{max} above the distal rim, which ticks up to ~0.015 m/s for the mid-flux ("strip") condition and reaches ~0.035 m/s for the high-flux ("spill") condition.

Circulation Cells

Overhead imagery (Mov. S1-3) and velocity measurements covering the river left hand side of the minibasins (Figs. 3&4) capture fluid circulation cells spawned from the current interaction with the

distal slope. We characterize fluid movement through minibasins using vector maps of the temporally averaged depth integrated fluid flux in the down and cross basin directions:

$$q_u = \int_0^H u dz \qquad [EQ. 2A]$$

$$q_v = \int_0^H v dz \qquad [EQ. 2B]$$

where H represents the current height, estimated with the integral length scale [*Ellison and Turner, 1959*] (Fig. 3A). Temporal averaging was done over the duration that the PCADP sampled each site. When vectors are scaled by input discharge, the structure of the discharge field is similar across experiments. High fluxes down the proximal slope efficiently deliver fluid and sediment to the center of minibasins. Down basin depth integrated fluxes then rapidly decrease going up the distal minibasin slope as fluid is routed into circulation cells. Due to the inlet flow entering the center of the basin in these experiments, the cells are laterally offset and positioned over the lower lateral slope.

Gradients in the velocity field of the flow adjusting to the confining minibasin describe local fluid stretching (strain) and rotation (vorticity). We quantify and compare the vorticity and strain rate at all sample points. From Dubief and Delcayre, 2000, the horizontal strain rate tensor is calculated from the symmetric part of the velocity gradient tensor as:

$$S = \tfrac{1}{2}[(\delta u/\delta x) + (\delta v/\delta y)] \qquad [EQ. 3]$$

and the horizontal vorticity is calculated from the asymmetric part of the velocity gradient tensor as:

$$\Omega = \tfrac{1}{2}[(\delta v/\delta x) - (\delta u/\delta y)] \qquad [EQ. 4]$$

where x and y are down and cross basin locations, respectively. We quantify and visualize strength of rotation relative to the lateral strain rate of the fluid using the Q-criterion, Q:

Positive Q indicates vorticity exceeds shear (strain rate tensor), and negative values represent areas where strain rate dominates the 3-D flow field [*Dubief and Delcayre, 2000*]. We hypothesize that circulation with positive Q at the cell center is associated with upwelling fluid, a consequence of fluid mass

conservation. This 3-D flow pattern would control sediment transport and deposition. Maps of Q at various minibasin depths highlight that the center of the circulation cell has vorticity that exceeds the strain rate (Fig. 3D-E). Here, we present results from the high-flux condition, which are similar in structure (but different in magnitude) to the other experiments. The center of the cell migrates laterally away from minibasin center with increasing minibasin height. While Q values indicate whether vorticity or strain rate is larger at a point, it does not inform on the fractional difference of the two. This can be estimated with the kinematic vorticity number [*Dubief and Delcayre, 2000*]:

$$\Omega_k^* = \frac{||\Omega||}{||S||} \qquad [EQ.\ 6]$$

We track vorticity, strain rate, and the w velocity component near the center of the circulation cell for all heights in the minibasin. The center of this cell laterally migrates away from minibasin center with increasing water depth. Near the center of the vortex, Ω^*_k is between 2 to 75, suggesting limited fluid stretching during rotation (Fig. 3B). This is associated with a profile of the w velocity component with upwards directed flow that considerably exceeds the still sediment fall velocity, w_s, of the median grain size introduced to the basin (0.5 mm/s) and the vertical detrainment velocity (Fig. 3C). This upwelling flow will influence sediment settling velocities as a function of the grain size distribution, leading to enhanced trapping potential of coarse, relative to fine, particles. However, the profile has considerable structure with significant upwards directed flow in the lower third of the current, that reduces to near zero in the middle of the flow. This reduction might be linked to low vertical shear at the u_{max} elevation [*Islam and Imran, 2010*]. The top third of the flow again is defined by upwelling flow that exceeds w_s.

We use velocity measurements to calculate flow streamlines. The streamlines capture horizontal gathering of flow into the center of the circulation cells and strong upwelling flow at the cell center (Fig. 4).

Minibasin margin onlap

Sedimentation patterns are characterized using isopach maps, calculated by differencing initial and final topography for an experiment. As a different total volume of sediment was released into the basin for each experiment, due to different flow discharges, we normalized deposition by the mean deposit thickness over the flat minibasins floor, D^* (Fig. 5A-C). While the structure of the concentration profiles at minibasin center might suggest similar gradients in deposition with distance up minibasin slopes, we observe stark differences between experiments in the deposit taper against slopes. Most of the sediment released into the low-flux experiment is contained within the minibasin, with deposit thickness at the minibasin rim only 10% of minibasin center thickness. In contrast, deposit thickness at the rim elevation exceeds 50% of minibasin center thickness for the high-flux experiment, highlighting the spilling nature of this experiment. Excluding data from the proximal slope, we quantify the rate of thinning up minibasin slopes by binning measurements of normalized deposit thickness by elevation above minibasin center, with 1 mm tall bins. Bin averaged data generate an average onlapping profile that is a function of normalized minibasin elevation, equal to elevation above minibasin center / minibasin depth, z^* (Fig. 5D). We use these profiles to calculate an onlap index, equal to the area underneath the curves in figure 5D:

$$I_o = \int_0^1 D^* dz^* \qquad \textit{[EQ. 7]}$$

Thus, sedimentation that does not change thickness up minibasin walls would yield an I_o of 1, while a linear decrease in sedimentation from minibasin center values to zero deposition on the minibasin rim would yield an I_o of 0.5. We measure I_o values of 0.48, 0.58, and 0.72 for the low, mid, and high flux experiments, respectively.

Discussion

A key finding of this study is the new observation of paired circulation cells resulting from turbidity currents interacting with minibasin topography (Mov. S1-3, Fig. 1B & 3-4). Velocities within these circulation cells vary as a function of input discharge. However, their structure, following

normalization, is remarkably similar over the fill-to-strip-to-spill spectrum (Fig. 3A). This structure is setup during the initial traverse of the turbidity current front, which does not fill the full minibasin width (Mov. S1-3). Reflection off the distal slope results in return flow along lateral minibasin slopes. This same structure is observed during equilibrium conditions, where inlet flow sends dye into the minibasin center with minimal widening until it reflects laterally when running up the distal slope (Mov. S1-3).

Prior 2-D experiments highlighted circulation in minibasins along a vertical plane (Fig. 1A) [*Patacci et al., 2015*]. During equilibrium conditions, we do not observe return flow at the center of the minibasin in the experiments reported here (Fig. 2). This suggests the ability of currents to laterally expand and setup circulation along a horizontal plane suppresses the development of circulation along a vertical plane. As a result, sediment charged flow that cannot escape over the distal rim is directed to and deposited on the lateral slopes.

Study of circulation cells in flows has a long history in sedimentology, including controlling the formation of river meanders [*Einstein, 1926*] and bedform development [*Gilbert, 1914*]. Here, the centers of minibasin circulation cells have positive Q-criterion indicating the importance of fluid rotation in ponded turbidity currents. The gathering of flow towards the center of cells (Fig. 4) drives upwelling with vertical fluid velocities that exceed the still fluid settling velocity of sediment introduced to the minibasins (Figs. 3C&4). However, vertical velocity profiles suggest sediment entering the lower portions of the vortex might not be able to transit to the flow top. This likely creates a sediment trap that enhances sediment concentrations until the flow wanes and sediment rains to the bed. This could be the reason for the thick deposits offset either side of minibasin center in the high-flux experiment (Fig. 5C). However, sediment entering the vortex in the upper third of the flow likely can escape the flow top, reducing basin sediment trapping potential relative to theory generated from 2-D minibasin experiments [*Lamb et al., 2006*]. Unfortunately, we do not have information on deposit particle sizes throughout the minibasin. However, we propose that circulation cells play a significant role in the fractionation of particulates, pollutants, and nutrients.

Deflection of flow running up the distal slope routes sediment laden flow over the lateral minibasin slopes, resulting in deposition throughout the minibasin (Fig. 1B). We highlight that sediment concentration profiles at minibasin center are similar for the three experimental conditions, but the onlap index, I_o, varies greatly between experiments (Fig. 5). We link this to varying degrees of flow runup onto distal minibasin slopes. We compare Δz resulting from runup to our onlap index and note a near linear trend (Fig. 5E). This supports that the degree of runup on the distal minibasin slope influences the amount of sediment delivered to circulation cells that then distribute sediment minibasin wide.

Finally, we note that the vertical flow structure captured in these experiments differs strongly from unconfined turbidity currents [*Altinakar et al., 1996; Sequeiros et al., 2010*]. Development of rules and theory emanating from 3-D experiments will aid future development of layer averaged models of turbidity currents interacting with complicated topography.

Conclusions and implications

As some of the largest sediment transport processes on the Earth surface, turbidity currents are critically important. Traversing the seafloor they are often subject to large topographic constraints, such as minibasins. Here new experimental methodology is developed and used to study the dynamics of turbidity currents as they interact as with three dimensional minibasin topography.

For the first time it is shown that three-dimensional flow structure generates inwards spiraling horizontal flow circulation cells, with strong central upwelling jets (Fig. 1B). Fluid rotation in these cells is significant, with vorticity exceeding the fluid's strain rate. Mass conservation at the center of circulation cells drives the upwelling. However, a dead zone of low vertical velocity separates regions where the velocity of upwelling fluid significantly exceeds the still fluid sediment fall velocity.

The dynamics presented here will both distribute and fractionate particulates, pollutants and nutrients transported by turbidity currents. Specifically, the ability for minibasins to act as a sink for microplastics and particulate organic carbon, which have low settling velocities, may be significantly reduced.

Acknowledgements

Support from grants to Reece from The Geological Society of America, American Association of Petroleum Geology, and by SEPM, Society for Sedimentary Geology; grants to Straub from The Tulane Carol Lavin Bernick Fund, ExxonMobil, The U.S. - Israel Energy Center funded through the Binational Industry Research and Development Foundation; and grants to Dorrell by the UK Natural Environment Research Council NE/S014535/1.

Data availability statement

Data that support this study can be downloaded at https://doi.org/10.5281/zenodo.8144554.

Figures

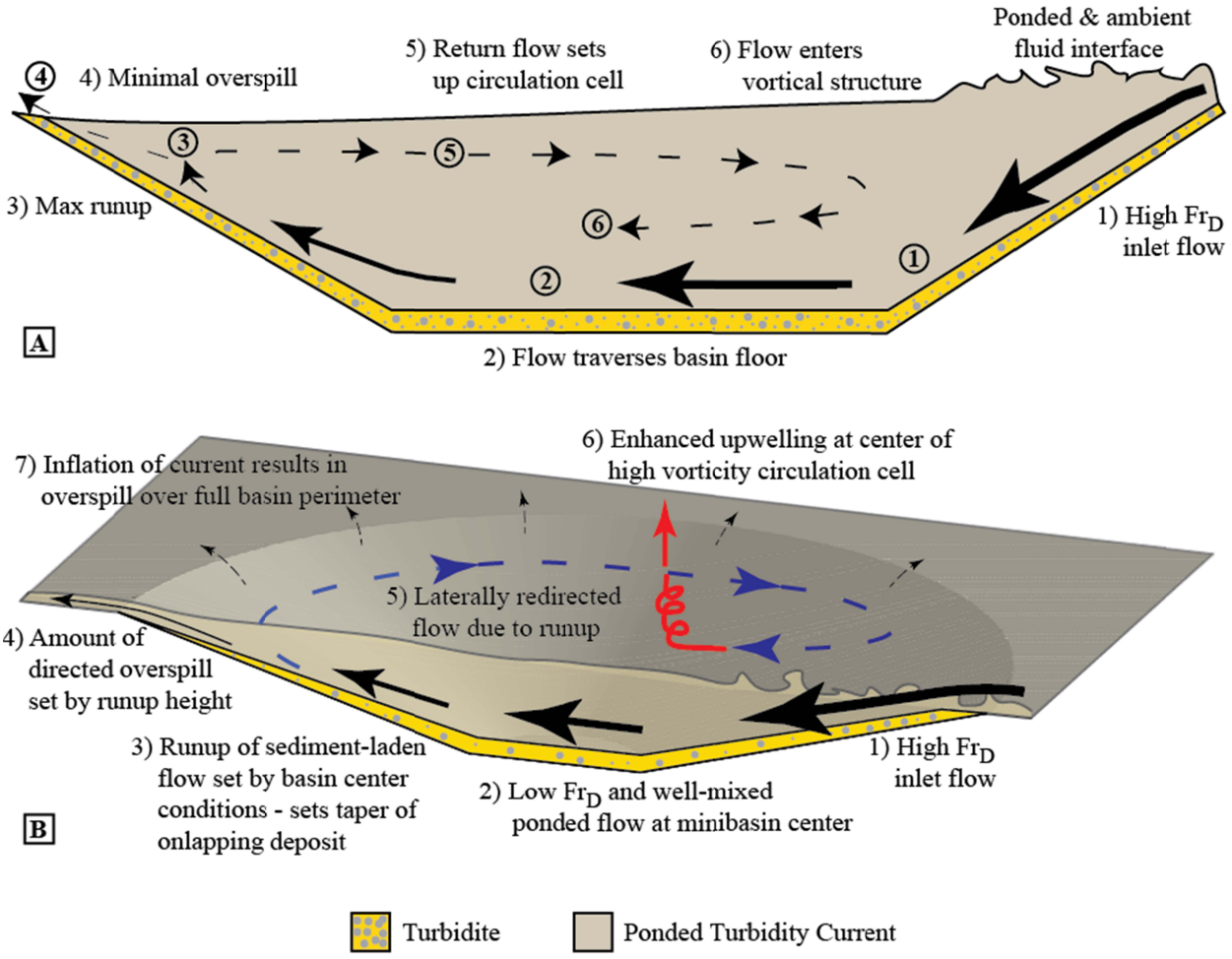

Figure 1. A) 2-D and B) 3-D schematics of circulation cell development inside topographically enclosed minibasins.

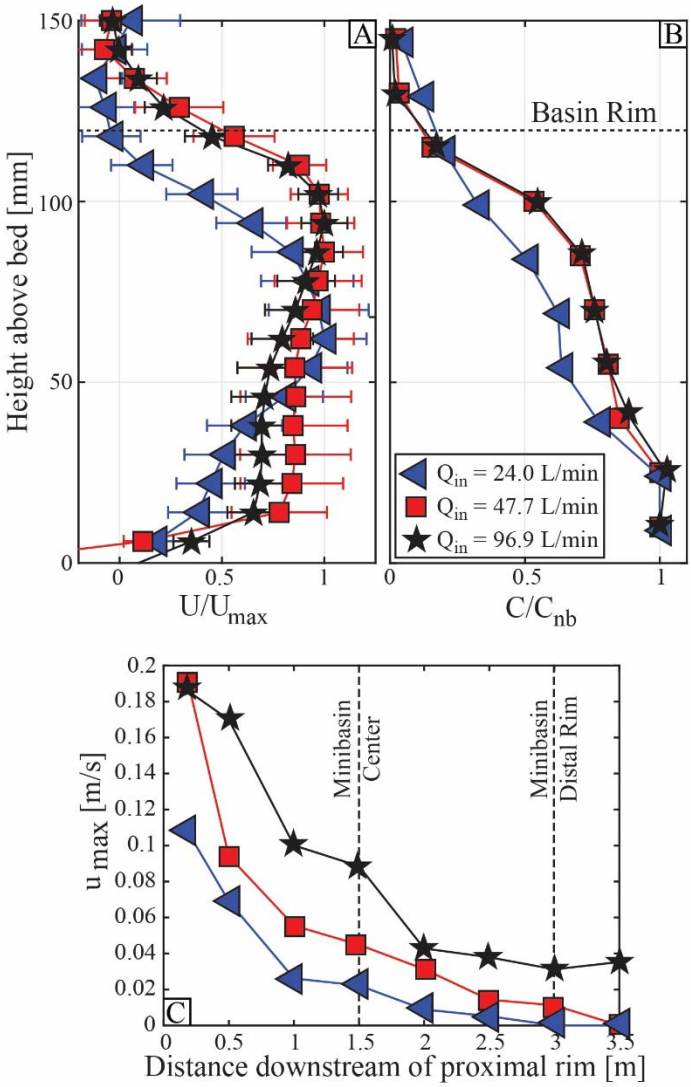

Figure 2. Velocity and concentration measurements at minibasin center and flow evolution along the down basin traverse. A-B) Profiles at minibasin center normalized by the maximum velocity in a profile and near bed sediment concentration, respectively. C) Measurements of the maximum velocity along the basin bisect line.

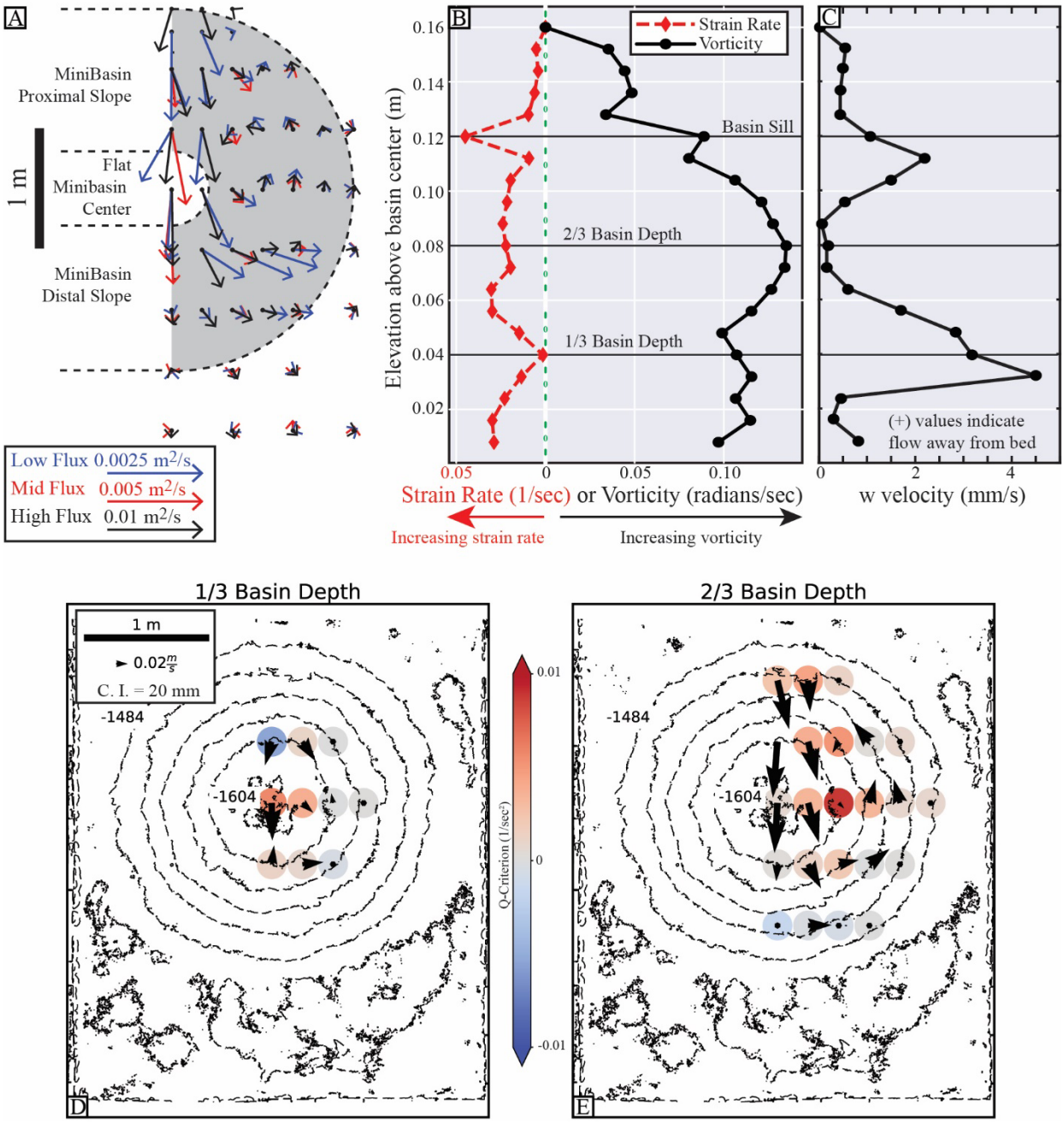

293

294

295 **Figure 3.** Characterization of minibasin three-dimensional velocity field. Primary flow direction in maps
296 is from top to bottom. A) Vector field of the depth integrated fluid flux. B) Magnitude of flow strain rate
297 and vorticity and C) *w* component of velocity as a function of elevation above floor of minibasin and
298 lateral position following center of circulation cell, which migrates away from basin center with
299 increasing flow height, as defined by the maximum Q-criterion. C-D) Measurements of Q-criterion

(colored dots) for the high-flux experiment along depth slices. Quivers show the *u* and *v* velocity components on each depth slice. Contours represent pre-flow topography.

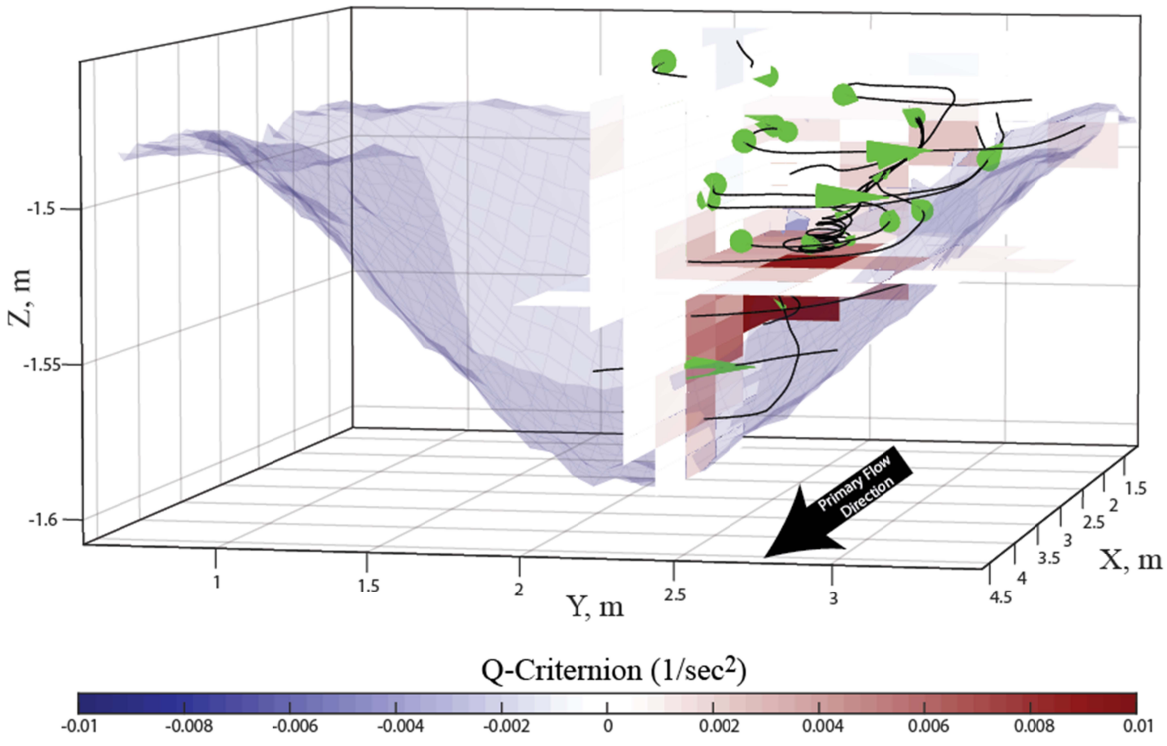

Figure 4. 3-D streamline and cone plots detailing flow structure in the high-flux experiment. Minibasin topography pre-flow is illustrated in semitransparent blue mesh, with distal basin topography excluded to aid visualization. 10x Vertical exaggeration applied to aid visualization. Horizontal and vertical slices display Q-criterion. Note upwelling and spiraling current at center of circulation that corresponds to the maximum Q-criterion values.

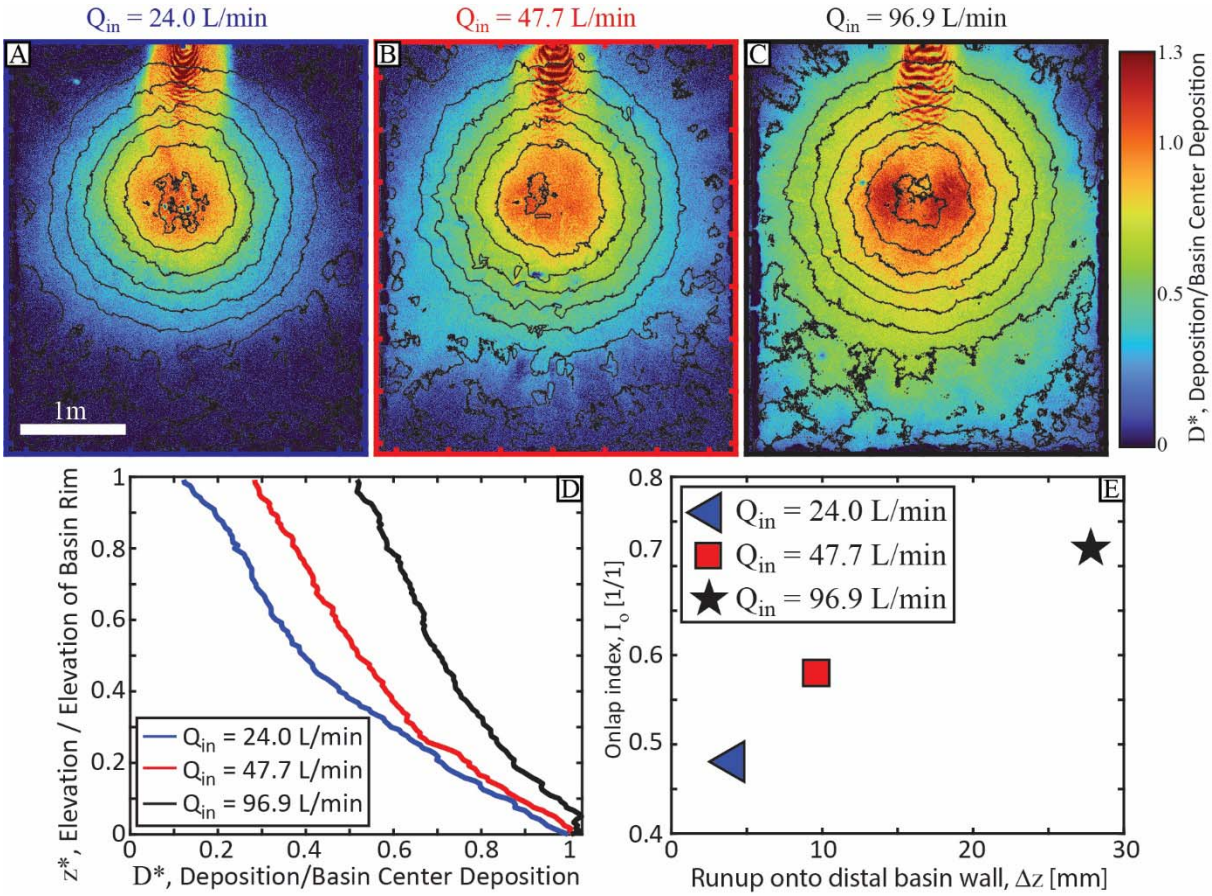

Figure 5. Measurements of sediment deposition and link to the turbidity current velocity field. A-C) Sediment isopach maps normalized by minibasin center conditions. Contours represent initial minibasin topography. Primary flow direction in all maps is from top to bottom. D) average sediment deposition profile up minibasin slopes. E) Cross-plot of estimated distal minibasin wall flow runup to onlap index.

References

Altinakar, M. S., W. H. Graf, and E. J. Hopfinger (1996), Flow structure in turbidity currents, *Journal of Hydraulic Research*, *34*, 713-718.

Azpiroz-Zabala, M., M. J. Cartigny, P. J. Talling, D. R. Parsons, E. J. Sumner, M. A. Clare, S. M. Simmons, C. Cooper, and E. L. Pope (2017), Newly recognized turbidity current structure can explain prolonged flushing of submarine canyons, *Science advances*, *3*(10), e1700200.

Badalini, G., B. Kneller, and C. D. Winker (2000), Architecture and Processes in the Late Pleistocene Brazos-Trinity Turbidite System, Gulf of Mexico Continental Slope, *GCSSEPM*, *20th Annual Research Conference Deep-Water Reservoirs of the World*, 16-34.

Bastianon, E., E. Viparelli, A. Cantelli, and J. Imran (2021), 2D numerical simulation of the filling process of submarine minibasins: Study of deposit architecture, *Journal of Sedimentary Research*, *91*(4), 399-414.

Beaubouef, R., and V. Abreu (2006), Basin 4 of the Brazos-Trinity slope system: Anatomy of the terminal portion of an intra-slope lowstand systems tract.

Beaubouef, R., and S. Friedmann (2000), High resolution seismic/sequence stratigraphic framework for the evolution of Pleistocene intra slope basins, western Gulf of Mexico: depositional models and reservoir analogs.

BOEM (2017), Northern GoM Deepwater Bathymetry Grid from 3D Seismic [Data file]. Retrieved from https://www.boem.gov/oil-gas-energy/mapping-and-data/map-gallery/northern-gom-deepwater-bathymetry-grid-3d-seismic.

Brunt, R. L., W. D. McAffrey, and B. C. Kneller (2004), Experimental modeling of the spatial distribution of grain size developed in a fill-and-spill mini-basin setting, *Journal of Sedimentary Research*, *74*(3), 438-446.

Carter, L., R. Gavey, P. J. Talling, and J. T. Liu (2014), Insights into submarine geohazards from breaks in subsea telecommunication cables, *Oceanography*, *27*(2), 58-67.

Dubief, Y., and F. Delcayre (2000), On coherent-vortex identification in turbulence, *Journal of turbulence*, *1*(1), 011.

Ellison, T., and J. Turner (1959), Turbulent entrainment in stratified flows, *Journal of Fluid Mechanics*, *6*(3), 423-448.

Fukuda, S., M. G. de Vet, E. W. Skevington, E. Bastianon, R. Fernández, X. Wu, W. D. McCaffrey, H. Naruse, D. R. Parsons, and R. M. Dorrell (2023), Inadequacy of fluvial energetics for describing gravity current autosuspension, *Nature Communications*, *14*(1), 2288.

Gilbert, G. K., and E. C. Murphy (1914), *The transportation of debris by running water*, US Government Printing Office.

Hage, S., V. Galy, M. Cartigny, S. Acikalin, M. Clare, D. Gröcke, R. Hilton, J. Hunt, D. Lintern, and C. McGhee (2020), Efficient preservation of young terrestrial organic carbon in sandy turbidity-current deposits, *Geology*, *48*(9), 882-887.

Islam, M. A., and J. Imran (2010), Vertical structure of continuous release saline and turbidity currents, *Journal of Geophysical Research: Oceans*, *115*(C8).

Khripounoff, A., A. Vangriesheim, N. Babonneau, P. Crassous, B. Dennielou, and B. Savoye (2003), Direct observation of intense turbidity current activity in the Zaire submarine valley at 4000 m water depth, *Marine geology*, *194*(3-4), 151-158.

Lamb, M. P., T. Hickson, J. G. Marr, B. Sheets, C. Paola, and G. Parker (2004), Surging versus continuous turbidity currents: flow dynamics and deposits in an experimental intraslope minibasin, *Journal of Sedimentary Research*, *74*(1), 148-155.
Lamb, M. P., H. Toniolo, and G. Parker (2006), Trapping of sustained turbidity currents by intraslope minibasins, *Sedimentology*, *53*, 147-160.
Maharaj, V. T. (2012), The effects of confining minibasin topography on turbidity current dynamics and deposit architecture.
Meiburg, E., S. Radhakrishnan, and M. Nasr-Azadani (2015), Modeling gravity and turbidity currents: computational approaches and challenges, *Applied Mechanics Reviews*, *67*(4).
Mitchum Jr, R. M., P. R. Vail, and J. B. Sangree (1977), Seismic stratigraphy and global changes of sea level: Part 6. Stratigraphic interpretation of seismic reflection patterns in depositional sequences: Section 2. Application of seismic reflection configuration to stratigraphic interpretation.
Patacci, M., P. D. Haughton, and W. D. Mccaffrey (2015), Flow behavior of ponded turbidity currents, *Journal of Sedimentary Research*, *85*(8), 885-902.
Pirmez, C., B. E. Prather, G. Mallarino, W. W. O'Hayer, A. W. Droxler, and C. D. Winker (2012), Chronostratigraphy of the Brazoz-Trinity Depositional System, Western Gulf of Mexico: Implications for Deepwater Depositional Models, in *Application of the Principles of Seismic Geomorphology to Continental-Slope and Base-of-Slope Systems: Case Studies from Seafloor and Near-Seafloor Analogues*, edited by B. E. Prather, M. E. Deptuck, D. Mohrig, B. Van Hoorn and R. B. Wynn, pp. 111-143, SEPM.
Pohl, F., J. T. Eggenhuisen, M. Cartigny, M. Tilston, J. de Leeuw, and N. Hermidas (2020a), The influence of a slope break on turbidite deposits: an experimental investigation, *Marine Geology*, *424*, 106160.
Pohl, F., J. T. Eggenhuisen, I. A. Kane, and M. A. Clare (2020b), Transport and burial of microplastics in deep-marine sediments by turbidity currents, *Environmental science & technology*, *54*(7), 4180-4189.
Prather, B. E., C. Pirmez, C. D. Winker, M. Deptuck, D. Mohrig, B. Van Hoorn, and R. Wynn (2012), Stratigraphy of linked intraslope basins: Brazos-Trinity system western Gulf of Mexico, *Application of the principles of seismic geomorphology to continental-slope and base-of-slope systems: Case studies from seafloor and near-seafloor analogues: SEPM, Special Publication*, *99*, 83-109.
Satterfield, W. M., and E. Behrens (1990), A late Quaternary canyon/channel system, northwest Gulf of Mexico continental slope, *Marine Geology*, *92*(1-2), 51-67.
Sequeiros, O. E., B. Spinewine, R. T. Beaubouef, T. Sun, M. H. García, and G. Parker (2010), Characteristics of velocity and excess density profiles of saline underflows and turbidity currents flowing over a mobile bed, *Journal of Hydraulic Engineering*, *136*(7), 412-433.
Soutter, E. L., D. Bell, Z. A. Cumberpatch, R. A. Ferguson, Y. T. Spychala, I. A. Kane, and J. T. Eggenhuisen (2021), The influence of confining topography orientation on experimental turbidity currents and geological implications, *Frontiers in Earth Science*, *8*, 540633.
Sparkes, R. B., I.-T. Lin, N. Hovius, A. Galy, J. T. Liu, X. Xu, and R. Yang (2015), Redistribution of multi-phase particulate organic carbon in a marine shelf and canyon system during an exceptional river flood: Effects of Typhoon Morakot on the Gaoping River–Canyon system, *Marine Geology*, *363*, 191-201.

Spinewine, B., O. E. Sequeiros, M. H. Garcia, R. T. Beaubouef, T. Sun, B. Savoye, and G. Parker (2009), Experiments on wedge-shaped deep sea sedimentary deposits in minibasins and/or on channel levees emplaced by turbidity currents. Part II. Morphodynamic evolution of the wedge and of the associated bedforms, *Journal of Sedimentary Research*, *79*(8), 608-628.

Toniolo, H., M. Lamb, and G. Parker (2006a), Depositional turbidity currents in diapiric minibasins on the continental slope: formulation and theory, *Journal of Sedimentary Research*, *76*(5), 783-797.

Toniolo, H., G. Parker, V. Voller, and R. Beaubouef (2006b), Depositional turbidity currents in diapiric minibasins on the continental slope: experiments—numerical simulation and upscaling, *Journal of Sedimentary Research*, *76*(5), 798-818.

Traer, M., A. Fildani, O. Fringer, T. McHargue, and G. Hilley (2018), Turbidity current dynamics: 1. Model formulation and identification of flow equilibrium conditions resulting from flow stripping and overspill, *Journal of Geophysical Research: Earth Surface*, *123*(3), 501-519.

van Andel, T. H., and P. D. Komar (1969), Ponded sediments of the Mid-Atlantic Ridge between 22 and 23 North latitude, *Geological Society of America Bulletin*, *80*(7), 1163-1190.

Violet, J., B. Sheets, L. Pratson, C. Paola, R. Beaubouef, and G. Parker (2005), Experiment on turbidity currents and their deposits in a model 3D subsiding minibasin, *Journal of Sedimentary Research*, *75*(5), 820-843.

Wang, X., S. M. Luthi, D. M. Hodgson, D. Sokoutis, E. Willingshofer, and R. M. Groenenberg (2017), Turbidite stacking patterns in salt-controlled minibasins: insights from integrated analogue models and numerical fluid flow simulations, *Sedimentology*, *64*(2), 530-552.

Winker, C. D. (1996), High-resolution seismic stratigraphy of a late Pleistocene submarine fan ponded by salt-withdrawal mini-basins on the Gulf of Mexico continental slope, paper presented at Offshore Technology Conference, OnePetro.

Yang, S., Y. An, and Q. Liu (2019), A two-dimensional layer-averaged numerical model for turbidity currents, *Geological Society, London, Special Publications*, *477*(1), 439-454.